

Numerical effects on the simulation of surfactant flooding for enhanced oil recovery

Olaitan Akinyele (✉ oa44@hw.ac.uk)

Heriot-Watt University Institute of Petroleum Engineering <https://orcid.org/0000-0002-7712-0161>

Karl D. Stephen

Heriot-Watt University

Research Article

Keywords: Reservoir simulation, Numerical dispersion, Surfactant flood, Oil recovery

Posted Date: October 5th, 2021

DOI: <https://doi.org/10.21203/rs.3.rs-180403/v1>

License: © ⓘ This work is licensed under a Creative Commons Attribution 4.0 International License.

[Read Full License](#)

Numerical effects on the simulation of surfactant flooding for enhanced oil recovery

Olaitan Akinyele

Heriot-Watt University, Petroleum Engineering, Edinburgh, Midlothian, United Kingdom

e-mail: Oa44@hw.ac.uk

0000-0002-7712-0161

Karl D. Stephen

Heriot-Watt University, Petroleum Engineering, Edinburgh, Midlothian, United Kingdom

e-mail: k.d.stephen@hw.ac.uk

Abstract

Numerical simulation of surfactant flooding using conventional reservoir simulation models can lead to unreliable forecasts and bad decisions due to the appearance of numerical effects. The simulations give approximate solutions to systems of nonlinear partial differential equations describing the physical behavior of surfactant flooding by combining multiphase flow in porous media with surfactant transport. The approximations are made by discretization of time and space which can lead to spurious pulses or deviations in the model outcome. In this work, the black oil model was simulated using the decoupled implicit method for various conditions of reservoir scale models to investigate behaviour in comparison with the analytical solution obtained from fractional flow theory. We investigated changes to cell size and time step as well as the properties of the surfactant and how it affects miscibility and flow. The main aim of this study was to understand pulse like behavior that has been observed in the water bank to identify cause and associated conditions. We report for the first time that the pulses occur in association with the simulated surfactant water flood front and are induced by a sharp change in relative permeability as the interfacial tension changes. Pulses are diminished when the adsorption rate was within the value of 0.0002kg/kg to 0.0005kg/kg. The pulses are absent for high resolution model of 5000 cells in x direction with a typical cell size as used in well-scale models. The growth or damping of these pulses may vary from case to case but in this instance was a result of the combined impact of relative mobility, numerical dispersion, interfacial tension and miscibility. Oil recovery under the numerical problems reduced the performance of the flood, due to large amounts of pulses produced. Thus, it is important to improve existing models and use appropriate guidelines to stop oscillations and remove errors.

Keywords

Reservoir simulation; Numerical dispersion; Surfactant flood; Oil recovery

Declarations

Funding: Nigerian Petroleum Technology Development Fund (PTDF)

Conflicts of interest/Competing interests: Not applicable.

Availability of data and material: Not applicable

Code availability: Eclipse 100 simulator

Authors' contributions: Not applicable

Ethics approval: Not applicable

Consent to participate: Not applicable.

Consent for publication: Not applicable

1 Introduction

An oil field development may be subdivided into three stages: appraisal, mature and late field development for oil recovery. Unfortunately, most of the world's oil fields have reached, or are approaching, the late field development phase that is a few years of the total recoverable field oil production before abandonment. At this point, secondary recovery has been exhausted and production may be considered as being no longer economically viable. Therefore, companies have explored alternative methods which are also referred to as tertiary, whereby oil is recovered by the injection of substances not naturally found in the petroleum reservoir. Chemical flooding is an important example of such a method. Chemical flooding techniques are often applied to alter fluid mobility and enhances the efficiency of the flood. This process is considered because conventional or secondary flood techniques have the potential to recover a third of the initial oil-in-place, leaving residual or by-passed oil in the reservoir. Therefore, it is crucial for companies to explore tools that are capable of modelling the physical phenomena as well as solving the resulting sharply changing fluid interfaces associated with such techniques to improve the field economic viability [1, 2].

Experimental and analytical modelling approaches have been used to formulate laws and correlations for chemical flooding techniques, which are used to predict fluid flow and frontal advances through a porous medium. Numerical modelling approaches use a gridded format that can accommodate any reservoir description. This is integrated with nonlinear, multiphase partial differential flow equations which cannot be solved by an analytical approach, except in limiting circumstances. Numerical models have been widely used as an inexpensive alternative to experimental or physical modeling to assist with decision making through reservoir simulators. Simulations help predict and optimize recovery from petroleum reservoirs. Over the years, commercial simulators have utilized proven computational advancements to combine systems of mathematical equations to describe the process of enhanced oil recovery with surfactant flooding, which is the focus of this study. Numerical stability and accuracy of the surfactant flood model are very important to accurately compare recovery techniques for oil production. Today simulations are used on a daily basis, with a degree of dependability of the solution. The simulators solve systems of nonlinear partial differential equations used to define the physical behaviors of surfactant flooding and recovery process. The simulations approximate the solutions by discretization of time and space which can lead to spurious oscillations, instabilities, or deviations in the model outcome [3]. The results may be used to predict or optimize oil production, so inaccuracies in the model could lead to false predictions, which can harm the economic valuation. Similar potential numerical issues may be encountered using the commercial simulator, which was documented in the simulator technical manual [4] with local grid refinements leading to numerical differences between the coarse and highly refined cases. Nevertheless, modelling and simulations are necessary tools in evaluating the practical application of surfactant flooding and potential implementation along with other chemicals.

2 Surfactant mechanism

Surfactant flooding has been studied in this paper and several mechanisms of recovery have been reported in the literature for over 40 years [5-12]. The recovery process is dependent on the injection of surfactants into the reservoir in a mixture along with injected fluid. The surfactant molecule has one end that is oleophilic and the other hydrophilic. The key mechanism therefore involves the fluid-fluid interface (oil and the displacing fluid), with the aim of reducing interfacial tension (IFT) and altering the capillary forces which influences the mobility of bypassed oil in the porous media. The surfactant flood mechanism for oil recovery decreases the IFT to recover mobilise oil that has been trapped by capillary forces during secondary recovery using water flooding. Thus, we can increase the capillary number (N_c), which is the dimensionless ratio of viscous to capillary forces to improve sweep and displacement efficiency. The relationship between the capillary number and oil-water IFT is given as follows [12]:

$$N_c = v\mu_w/IFT_{ow} \quad (1)$$

where v is the interstitial velocity of water, μ_w is the aqueous phase viscosity and IFT_{ow} is the oil-water interfacial tension also referred to as IFT.

Observations [13, 14] have shown surfactant flooding improves the displacement efficiency when used after secondary recovery, a higher N_c results in a larger quantity of bypassed oil being extracted, which can be around 60% of the original oil in place [15]. In water flooding, the N_c is usually 10^{-9} to 10^{-7} . The surfactant chemical interaction leads to a decrease in IFT and hence an increase in N_c , and likewise, oil recovery will increase significantly. Ideally, an improvement of N_c to 10^{-3} can recover 100% of oil in place. The surfactant may reduce the oil-water IFT from typical levels of 20-50 mN/m, down to 10^{-2} to 10^{-3} mN/m, thus yielding an improved displacement efficiency.

The change of capillary number has a corresponding impact on the relative permeability curve that is derived in core floods or used in simulations. Initially, the reservoir condition is such that water is immiscible with oil and relative permeability curves reflects that. At infinite capillary number, relative permeability curves are linear while they typically lie below the line for waterflooding. In addition, the residual oil is much reduced. If the capillary number can be increased from low to high values, so that the water becomes miscible, linear relative permeability curves are applicable. This also happens when surfactant is introduced. Several experiments reveal that a high capillary number of about 10^{-3} can enhance the recovery substantially, whereas a lower capillary number of $10^{-5.5}$ would not improve recovery [16].

3 Modelling of surfactant flooding

The surfactant flood will need to be modelled as an IFT altering effect to recover residual oil. This process is represented through the change of miscibility via the relative permeability curves [4]. In Fig. 1, the waterflood relative permeability curves are K_{ro} (orange) for oil and K_{rw} (blue) for water. At infinite N_c , the straight-line curves are used (K_{rw_surf} , yellow and K_{ro_surf} , grey, for water and oil respectively). Since the relationship between surfactant concentration and IFT calculation was unveiled [17, 18], surfactant transport models have been widely used in both analytical and numerical models for surfactant flooding to quantitatively analyze the mechanisms [19, 20].

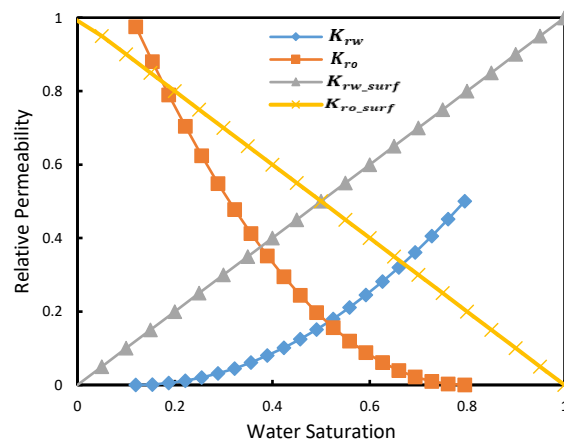


Fig. 1 Characteristic set of miscible and immiscible relative permeability curves of the oil-water and surfactant influenced system. Miscible flow consists of the mixture of oil and the displacing fluid which is a result of low interfacial tension between the oleic and aqueous phase. A single phase is formed, which significantly lowers the amount of bypassed oil. The term immiscible refers to the flow where water cannot be mixed with oil.

The surfactant concentration C_o influences the change in oil-water IFT, which causes a switch in the relative permeability curves. The immiscible set of relative permeabilities curves, denoted by K_{rw} , and K_{ro} , are applied in the absence of surfactant. With the influence of surfactant, the miscible relative permeabilities curves, denoted by K_{rw_surf} , and K_{ro_surf} are applied. Along with the switch from immiscible to miscible relative permeability curves, the surfactant contributes to the combined effect

of the IFT, and aqueous phase viscosity. Firstly, the IFT is calculated using a function equivalent to that shown in Fig. 2. The IFT_{ow} is initially at 0.05 N/m when there was no surfactant concentration in the solution. The critical micelle concentration (CMC) is achieved at the lowest IFT_{ows} value with surfactant concentration of 1kg/sm³. Once the CMC is achieved, the IFT remains constant with an increase in surfactant concentration. Meanwhile, the aqueous phase viscosity increases linearly with the surfactant concentration to the highest value of 5cP.

The relative permeability curves reflect the miscibility as a function of capillary number and is dependent and controlled by the interpolation parameter F_{kr} . This term is calculated from the logarithm (base 10) of the capillary number and can be used to define an instantaneous switch between the set of relative permeability curves. However, this instantaneous switch may lead to convergence problems, slowing the calculations and even produces numerical effects in form of oscillations and pulses in the solution. Consequently, a lower threshold of F_{kr} equivalent to zero, results in the immiscible flow. Whereas for the upper threshold of F_{kr} equal to one, the flow becomes a miscible displacement. In between these limits, the curves in Fig. 1 are interpolated using F_{kr} as a linear weighting in relation to the two limits.

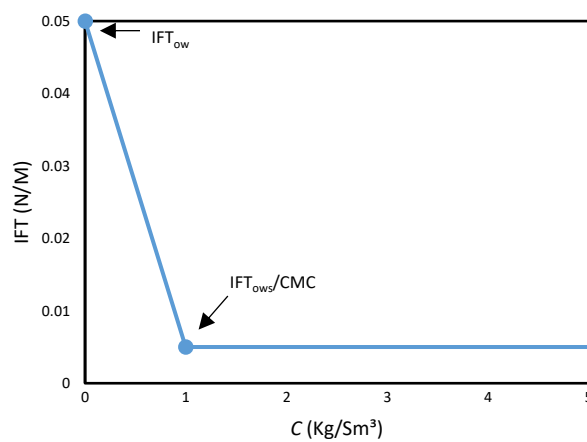


Fig. 2 Oil-water IFT at several surfactant concentration C , showing low oil-water IFT achieved with a low surfactant concentration [4].

It is very important for the prediction of surfactant flooding that the fronts are resolved accurately, which can be studied through the fractional flow theory [21, 22]. We illustrate the fractional flow function $F_w(S_w, C, F_{Kr})$ for certain combinations of surfactant concentration, C , and F_{Kr} written as (also plotted in Figure 3):

$$F_w(S_w, C, F_{Kr}) = \begin{cases} F_w(S_w, 0, 0), & \text{if } C = 0 \text{ and } F_{Kr} = 0 \\ F_w(S_w, 1, 0), & \text{if } C = 1 \text{ and } F_{Kr} = 0 \\ F_w(S_w, C_o, 1), & \text{if } C = C_o \text{ and } F_{Kr} = 1 \end{cases} \quad (2)$$

where C_o is the maximum concentration of surfactant and is equivalent to that of the injected water. the $F_w(S_w, 0, 0)$ is the fractional flow function for a normal waterflood, $F_w(S_w, 1, 0)$ is the fractional flow as if the surfactant concentration has reached 1kg/Sm³ without any change from the immiscible waterflood relative permeability behavior. Therefore, $F_w(S_w, 0, 0)$, $F_w(S_w, 1, 0)$ and $F_w(S_w, C_o, 1)$ are the fractional flow functions given by

$$F_w(S_w, 0, 0) = \frac{K_{rw}(S_w)}{K_{rw}(S_w) + \left(\frac{\mu_w}{\mu_o}\right) * K_{ro}(S_w)} \quad (3)$$

$$F_w(S_w, 1, 0) = \frac{K_{rw}(S_w)}{K_{rw}(S_w) + \left(\frac{\mu_w(1)}{\mu_o}\right) * K_{ro}(S_w)} \quad (4)$$

$$F_w(S_w, C_o, 1) = \frac{K_{rw_surf}(S_w)}{K_{rw_surf}(S_w) + \left(\frac{\mu_w(C_o)}{\mu_o}\right) * K_{ro_surf}(S_w)} \quad (5)$$

The surfactant solution is modelled as a single solute dissolved in water and alters the viscosity, μ_w , to stabilize the flood front and improve sweep efficiency. The influence of the surfactant concentration may be examined via the fractional flow curves (See Fig. 3). The value of the surfactant adsorption can be observed through the constant D_i , which is achieved through the use of the Welge tangent on the fractional flow curve as seen in Fig. 3 [19].

Fractional flow theory can be used to represent flow in a 1-D homogenous reservoir, neglecting the effects of gravity, capillary pressure, and physical dispersion [22]. This can provide a mathematical prediction of the physical transport of fluids and concentration through the porous medium, including the chemical reaction on the rock surface. We acknowledge this analytical solution will be acceptable for coarse-scale models in which the pressure difference from the viscous forces is usually much larger than from capillary forces. owing to high flow rates.

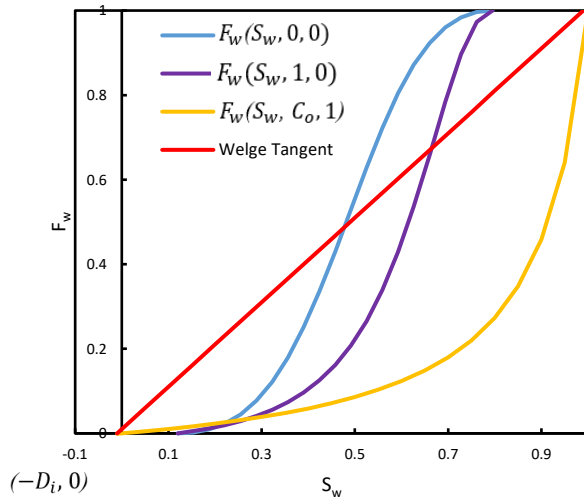


Fig. 3 Fractional flow curves based on the relative permeability curves (See Fig. 1) for an immiscible waterflood, $F_w(S_w, 0, 0)$ (blue line), immiscible surfactant flood with viscosity increase $F_w(S_w, 1, 0)$ (purple line), miscible $F_w(S_w, C_o, 1)$ (orange line) and Welge tangent $(-D_i, 0)$ applied to the surfactant fractional flow curve (red line). In the above example $D_i = -0.01$.

Researchers [19-26] have examined the dispersion of the surfactant solute front, involving numerical and physical dispersion at the core scale. However, owing to the fact that physical dispersion is ever so often offset by numerical dispersion; the first is ignored. We use the Peclet number to characterize dispersion.

$$N_{pe} = \frac{vx}{D} \quad (6)$$

The value of $N_{pe} \ll 1$ indicates dispersion dominates and advection is negligible. When $N_{pe} > 10$ advection dominates on the other hand and spreading is almost non-existent. If $N_{pe} \sim 1$ then neither dominates over the other and no approximation to the equation can be justified.

D in Eq. 6 is given by:

$$D = \alpha_{total} * v \quad (7)$$

We assume molecular diffusion to be insignificant in comparison with the dispersion. The total dispersivity α_{total} represents a combination of physical and numerical dispersion [22].

$$\alpha_{total} = \alpha_{physical} + \alpha_{Numerical} \quad (8)$$

Where $\alpha_{physical}$ is derived from continuous experimentally or field test measurement and to be zero for this research. While $\alpha_{Numerical}$ can be estimated by:

$$\alpha_{Numerical} = \left(\frac{\Delta x}{2} \pm \frac{v\Delta t}{2\phi} \right) \quad (9)$$

For grid block sizes Δx , timestep Δt and ϕ is porosity and the arithmetic subtraction operator (-) applied for Implicit Pressure-Explicit Saturation (IMPES) procedure and addition operator (+) for the fully implicit procedure [23]. The decoupled implicit scheme was used in this study such that physical dispersion is neglected. Eqn. 10 can be further simplified for the fully implicit Peclet number to obtain [27]:

$$N_{pe} = \frac{x}{\left(\frac{\Delta x}{2} \right) + \left(\frac{v\Delta t}{2\phi} \right)} \quad (10)$$

N_{pe} is used to evaluate numerical problems that may arise from the transport calculations due to overly large timesteps and cell sizes. The numerical effects lead to smeared spatial gradients of saturation and concentrations as well as grid orientation effects. The problem results from the truncation error in calculating the movement of saturation fronts as if additional physical dispersion were present. We will also show that other effects include pulses in fractional flow and saturations. Unfortunately, in explicit schemes, instabilities are apparent when the combination of Δx and Δt violates the numerical stability criterion [23]. These instabilities can lead to behavior not unlike that which we will report. However, it is not our contention that we are observing instabilities.

In the literature [23] for a sufficient small timestep in which the level of numerical dispersion is due to the spatial term, the level of dispersivity inbuilt in the simulator ought to be about half of the grid block size. The Courant-Friedrichs-Lewy found instability issues due to the time step effect, and to mitigate such problems, the Courant condition was derived to suggest a formulation for a time step size of each grid cell at a known fluid velocity and cell size. We would like to highlight that this condition was derived for an explicit scheme whereas this study used a decoupled implicit scheme that appears to have some numerical issues. To examine the stability of the numerical solution in the Surfactant flood model, we assume Equation.11 as the limit, and to ensure our model is an advection dominated system. The timestep limit can be given as [25]:

$$\Delta t_{Max} \leq \frac{\Delta x}{v} \quad (11)$$

where the v is the advection velocity.

As mentioned earlier, the key mechanism of the surfactant is alteration of interfacial tension, influenced by the level of adsorption. The adsorption level makes the process less efficient and also alters the Welge tangent points across the fractional flow curve, which influences change in the fluid flow behavior and directly affects the velocities of surfactant induced and formation water fronts. This is incorporated in the numerical modeling approach to impact the changes in the concentration distribution and mobilization of residual oil in the reservoir. Therefore, it is important to study and test the role of adsorption on the sharpening of the front and numerical solutions.

Modeling the impact of adsorption on the surfactant flood is captured by using a Langmuir-type isotherm. Adsorption is linear for small values of surfactant concentration but approaches a constant at high values. The analytical adsorption function allows for dependencies of adsorption on the rock permeability, salinity, and surfactant concentration [4]:

$$C_{ads} = \frac{a c^m}{1+bc} \quad (12)$$

$$a = (a_1 + a_2 C_{se}) \left(\frac{K_{ref}}{K} \right)^n \quad (13)$$

Where C_{ads} is the rock adsorbed concentration, C is the concentration in the solution surrounding the rock, m is an exponent for concentration dependence, C_{se} is the effective salinity for surfactant concentration, K is the grid block permeability, K_{ref} is the reference permeability, n is an exponent for permeability dependence, while a_1 , a_2 , b are adsorption coefficient input parameters for the simulation. The surfactant model range of adsorption can be evaluated using the retardation equation:

$$v_{ci} = \frac{v}{R_{ci}} \quad (14)$$

where R_{ci} is the retardation factor, v is the advection velocity of water and v_{ci} is the concentration velocity. Using the equations above we could evaluate a relationship between adsorption and numerical effects. We can use the analytical solution as a baseline to study adsorption effects and estimate the numerical effects on 2D and 3D models.

An algorithm for numerical stability analysis, based on the perturbation method, was developed by Druetta et al. [3] to ensure convergence in a two-phase, three-component system. The approach is appropriate for two-dimensional models; however, one must account for the impact of the surfactant mechanisms such as how adsorption may influence the precision of the solution.

Using numerical analysis, Al-Ibadi et al., [28-30] reported the propagation of pulses within the cells as numerical errors and highlighted the importance of precision for low salinity waterflooding. A similar approach is used in those models to switch relative permeability curves as salinity is reduced. This can induce a sharp increase of the flow of oil from a cell with reduction in water and creates a pulse. Simulation of surfactant flooding is dependent on the logarithm of the capillary number, influenced by the ratio of viscous to capillary forces and a sharp change to the relative permeability can also be induced.

Nevertheless, experiments have demonstrated that the synthesis of low surfactant concentration with new chemicals can achieve ultra-low IFT values and acceptable adsorption levels for EOR. Therefore, it is necessary to study how this type of flow might cause numerical problems in form of pulses that influence incorrect results. The overall goal is to present design consideration for surfactants aimed to attain low interfacial tension at low surfactant concentration, as well as low adsorption levels on the rock surface to recover bypassed oil saturation [31, 32].

4 Description of the simulation model

We began with a simple homogeneous 1D model solved through the black oil commercial simulator [4] to evaluate the flow behavior of the surfactant flood. The dimensions of the reservoir setup are 500m long, 500m wide, and 1.89m thick. The model was chosen to provide the simplest possible illustration of surfactant flooding, to streamline the interpretation of the flow behavior in a reservoir. One injection well was used with a production well at the extreme ends of the grid block in the x-axis, and both are completed vertically and fully perforated in all the interconnecting grid cells.

The base case model was represented with 100 cells, each defined in the x-direction. Models were tested with a range of timesteps to consider the influence of numerical dispersion based on the timestep alone. We further compared the impact of grid refinement on the numerical solution profile against the analytical models which predict the shock front behavior [22, 33]. The displacing fluid consisted of an aqueous phase, a mixture of water and the surfactant solution, where the injected surfactant increased the viscosity of the displacing fluid and reduced IFT between the oil and aqueous phases. Some features of the reservoir characteristics for the surfactant flood model were considered constant and due to the large dimensions of the model. Gravity, and capillary pressure effects were considered negligible compared to the viscous forces. These assumptions simplified the model and removed their impact on the numerical dispersion. The model used isotropic permeability to achieve the desired pressure limit. A commercial simulator [4] was used to solve the aqueous phase solutions simultaneously with

surfactant solute transport and all related equations using the decoupled implicit finite difference scheme.

The simulation models were studied using the rock and fluid properties along with the reservoir conditions as tabulated in Table 1. To focus on the surfactant flood solution, the water, and surfactant slug was injected from the beginning as a secondary process, through the injection well sweeping the mobilized oil to the production well. The injection rate was constant at $400 \text{ rm}^3/\text{day}$. Time step and grid size were our primary objective to evaluate the appearance of numerical effects and impact on solution accuracy.

5 Simulations of surfactant flooding

In this work, we evaluated the stability, precision, and efficiency of the numerical model and the components that influence the flow of surfactant flooding. The precision is termed as the minimal deviation of the solution affected by the numerical problem when compared to the exact partial differential equation that represents flow. Meanwhile, instability occurs when numerical effects result in a divergence of the numerical solution as a function of small perturbations. The numerical effects, also known as numerical dispersion, may also result in pulses and convergence problems [28-30]. They may be imprecise but stable, nonetheless. The efficiency of the numerical model refers to the simulator's ability to solve a wide range of physically distinct problems. The computational efficiency of the solution scheme accounts for the number of numerical values computed after the required "Newton iterations" per timestep and the time it took to solve the linearized system on each iteration.

Firstly, we evaluated the numerical solution of four models which consist of coarse ($10 \times 1 \times 1$), base case ($100 \times 1 \times 1$), refined ($1000 \times 1 \times 1$) and high-resolution ($5000 \times 1 \times 1$) block setup with time step defined according to the Courant condition, and compared to the solution obtained by fractional flow theory for surfactant flooding. The advection velocities of the surfactant-induced and formation waterfronts are 1.9m/day and 2.7m/day , respectively. We obtained solutions for various timesteps and obtained the Numerical dispersion and Peclet number (See Table 2).

The example showed the appearance of numerical effects in the form of pulses (Fig. 4 and 5) and a shifting of the surfactant concentration (Fig. 6) and viscosity behavior (Fig. 7). The high-resolution solution ($N_{pe} = 2000$) tends to follow that of the fractional flow theory as the decrease in the cell size to 0.1 m and time step of 0.04 days produced a sharp front in the water cut (See Fig. 4). The injected water front travelled at $S_w=1$ and $f_w=1$. The formation water front moved ahead of that at lower saturation and fractional flow values given by the Welge tangent which passes through the blue curve in Fig. 3 to $-D_i$ on the saturation axis.

An increase of the cell size to 0.5m and time step to 0.18 days in the refined solution ($N_{pe} = 400$), introduced numerical effects in the form of small pulses in the plateau (oil bank) with low amplitude reducing the precision of the result compared to the water cut solution obtained from fractional flow theory (Fig. 5). The base case ($N_{pe} = 40$) with a cell size of 5m and a time step of 1.82 days was observed to show higher pulse amplitude and longer wavelength, which caused an even greater deviation in the water cut compared to the refined and high-resolution water cut profile. A further increment of the cell size to 50m and time step to 18.24 days as observed in the coarse model ($N_{pe} = 4$) is shown in Fig. 5. The flow behavior tended to lose numerical precision due to the pulses which had significantly higher amplitude on the formation water plateau and failed to match the analytical solution. The coarse model also produced formation water breakthrough slightly earlier and the surfactant showed a more dispersed front due to larger cells.

The displacement profile of the surfactant concentration (Fig. 6) was obtained numerically from the cell closest to the production well, with a comparison of the corresponding effect on the effective aqueous phase viscosity (See Fig. 7) and the oil-water IFT (See Fig. 8). The analytical solution of the surfactant concentration was very similar to that obtained from refined ($N_{pe} = 400$) and high resolution ($N_{pe} = 2000$) but with a slight deviation in the base case ($N_{pe} = 40$). We observed that the numerical solution for the coarsest model was highly imprecise due to the combined effect of oil-water IFT and solution viscosity combining with numerical dispersion from the discretization errors. This effect may be seen through the earlier IFT change at 0.8 PVI for the coarse model compared to other models at approximately 1.1 PVI (See Fig. 8). Increasing the cell size had a large effect on dispersion of

surfactant. However, this mixed within the formation water in this case. While viscosity increased and the miscibility changed, the general speed of the injected water front was largely unaffected by comparison although the second water front did rise more slowly.

Table 1 Simulation Model Properties

Rock and fluid properties		Oil	Water		
Porosity	0.25	Reference Pressure - P_{ref} (bar)	200	270	
Permeability (md)- k_h	4500	Density (kg/m3) at Surface condition	850	1000	
		Viscosity (cP) at P_{ref}	0.47	0.34	
S_{or}	0.205	Formation volume Factor (rm3/sm3)	1.0	1.030	
Scaled Immiscible end-points	Scaled Miscible end-points	Surfactant Solution properties			
Critical Water Saturation - S_{wcr}	0.225	Surfactant Critical Water Saturation - SS_{wcr}	0.05	Injected Surfactant Concentration - $Surf_{conc}$ (kg/sm3)	30
Maximum water Saturation - S_{wu}	0.805	Maximum water Saturation - SS_{wu}	0.995	Solution water viscosity (cP) at $Surf_{conc}$	5
Connate Water Saturation - S_{wc}	0.12	Surfactant Connate Water Saturation - SS_{wc}	0.05	Water/oil surface tension at $Surf_{conc} = 0$	0.05
oil relative permeability - k_{ro}	0.975	surfactant oil relative permeability - Sk_{ro}	0.9	Water/oil surface tension at $Surf_{conc} = C_o$	1.0E-6
water relative permeability - k_{rw}	0.5	surfactant water relative permeability - Sk_{rw}	0.9	Surfactant adsorption (kg/kg) at $Surf_{conc}$	0.0005

Table 2 Computational times and Numerical Peclet number of the maximum timestep (Courant condition) for the increasing amount of grid cells and case identification.

Case ID.	Cells	Δx (m)	Δt_{Max} (days)	N_{pe}	CPU Time (seconds)
Coarse	10 x 1 x 1	50	18.24	4	34.9
Base case	100 x 1 x 1	5	1.82	40	76.1
Refined	1000 x 1 x 1	0.5	0.18	400	540.7
High-resolution	5000 x 1 x 1	0.1	0.04	2000	1343.8

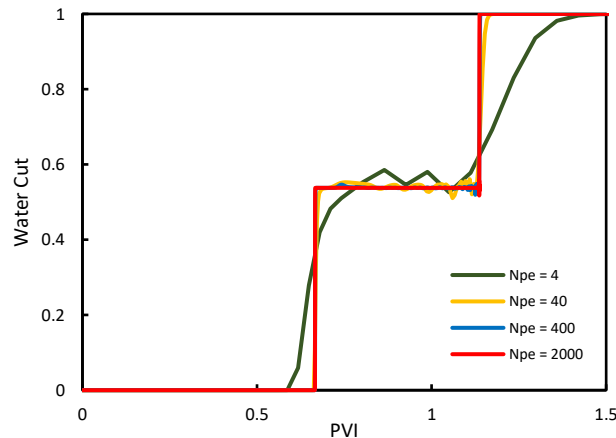


Fig. 4 A comparison of the produced water cut profile from the simulation results. The red line is the reference case in agreement with the fractional flow theory, $\Delta x = 0.1m$, $\Delta t_{Max} = 0.04$ days and TCPU = 183.6 s. The blue and orange lines show increased cell sizes of $\Delta x = 0.5$ m and $\Delta x = 5$ m, respectively. The green line shows a deviation from the reference case with $\Delta x = 50$ m, $\Delta t_{Max} = 18.24$ days and TCPU = 94.6 s.

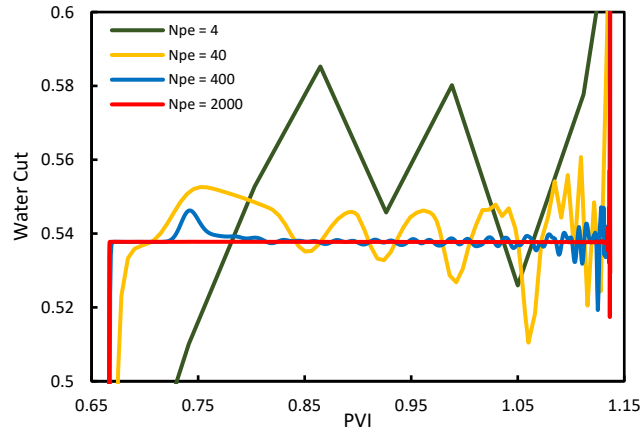


Fig. 5 A magnified representation of the comparison of the appearance of numerical effects for the various values of N_{pe} verse pore volume injected.

To show how the variation in effective surfactant concentration may lead to unfavorable flow, the coarse model at 1.5 PVI could be seen to reach viscosity of 5 cP with far lower concentration of $27\text{kg}/\text{sm}^3$ in comparison to the accurate input value of $30\text{kg}/\text{sm}^3$ as achieved in the base case, refined and high-resolution models. The effective surfactant concentration also triggered the change in miscibility, which is a function of the logarithm of the capillary number. Therefore, imprecise values of the effective surfactant concentration will lead to false values of the oil and water relative permeabilities, impacting the precision and stability of the model.

The relative advance of the surfactant profile as the cells were increased in size depends on the balance between dispersion and adsorption. With less adsorption we anticipate that it would advance faster. If it moves as fast as the head of the formation water front then more complex behavior could be seen, particularly if there is little adsorption or more dispersion.

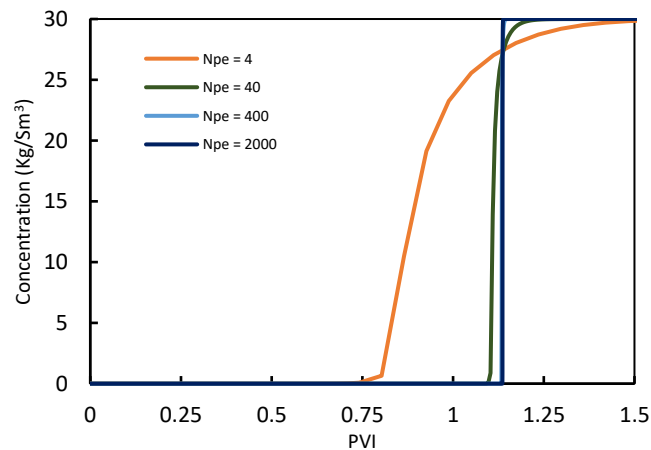


Fig. 6 Comparison of the surfactant concentration predicted for the producer versus the pore volume injected as derived from the simulator output with N_{pe} equal to 4 (orange line), 40 (green line), 400 (blue line), and 2000 (purple line).

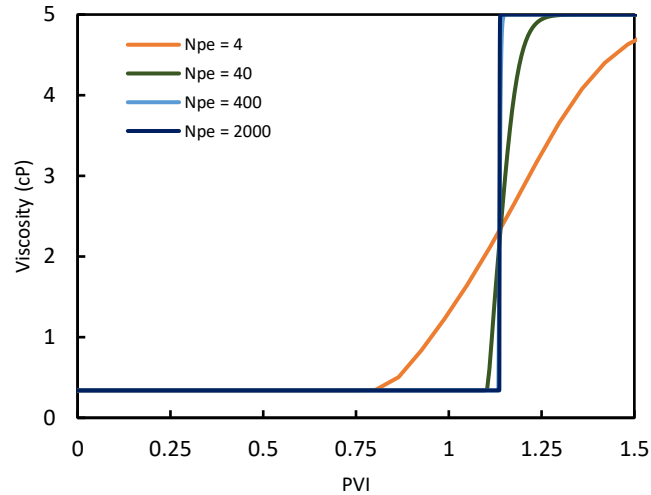


Fig. 7 Comparison models of the effective water solution viscosity versus the pore volume injected as derived from the simulator output with N_{pe} equal to 4 (orange line), 40 (green line), 400 (blue line), and 2000 (purple line).

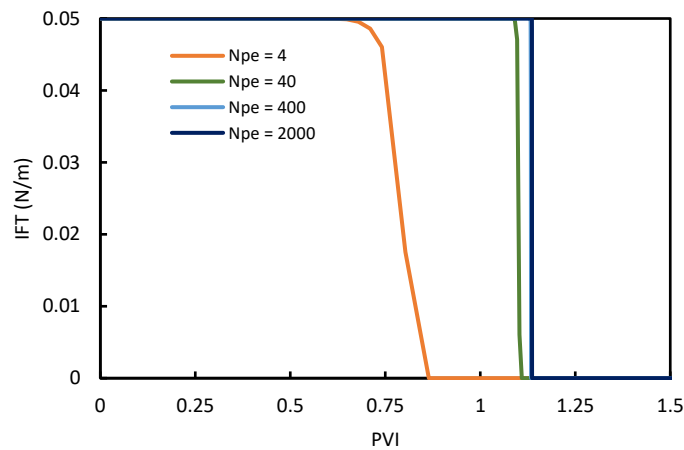


Fig. 8 Comparison of the oil-water IFT in produced water versus the pore volume injected as derived from the simulator output at the different values of N_{pe} equal to 4 (orange line), 40 (green line), 400 (blue line), and 2000 (purple line).

Besides precision, any significant improvement in the time-step domain would require an adaptive step solver, which would involve a larger computational time. The precision must be weighed against computational efficiency. The error in the coarsest model renders it useless as a tool for predicting behavior. The origin of this numerical effect on the fluid flow behavior is further evaluated through the mobility analysis in the grid cells and parameters influencing the numerical computation of the surfactant flood model.

6 Numerical computation of the mobility and weighting function

We examined the origin of the numerical effects from the coarse model (10 cells). We evaluated the dynamic behavior of relative permeability, saturation, $\log(N_c)$ and also the fractional flow (into the downstream cell) on a cell by cell basis (Fig. 9). The simplified fractional flow was obtained by the ratio of water flow rate to the total flowrate rate with a value between 0 and 1.

The relative permeability of water and oil and the fractional flow (Fig.9) was observed to have pulses which grew progressively as each cell transitioned from immiscible to miscible behavior and also as the viscosity changed. Similar effects have been reported previously albeit for low salinity

waterflooding [28-30] where the change in relative permeability (wettability) as a function of salinity appeared to generate equivalent pulses. We adopt a similar analysis and interpretation here.

Water saturation in the first cell ($i=1$) increased quite quickly reaching a maximum value at 0.2 PVI (Fig. 9a). The surfactant concentration also increased (Fig. 9b) and IFT was reduced. There was an initial change in K_{rw} (Fig 9c) and K_{ro} (Fig. 9d) at around 0.02 PVI when we see the $\log(N_c)$ passed through the transition, switching flow from immiscible to miscible behavior (Fig. 9e). The change to fractional flow (Fig. 9f) occurred slightly later as the viscosity in the cell changed.

The rise in saturation in the second cell occurred slightly later as the front moved with finite speed. Formation water was mobilized ahead of the front. There is a slight “kink” in the water saturation at around 0.1 PVI. Numerical dispersion caused the surfactant concentration to start to spread out. We see that the relative permeability to water shows a slight plateau around this time. This was coincidental with the rise in $\log(N_c)$ as IFT dropped and flow behavior became immiscible. The viscosity then rose (as it did in $i=1$) creating a broader plateau in the fractional flow.

This process continued as the fluid fronts moved through the reservoir. The formation front moved faster than the later high viscosity surfactant front creating a plateau in saturation which spread out. Each cell saw a minor increase in $\log(N_c)$ ahead of the main surfactant front as formation water then a sharp switch in as the fluids become miscible. The initial rise in $\log(N_c)$ was due to the mobilization of the formation water and a change to the interstitial velocity. The water relative permeability jumped up with the switch to miscibility as did oil relative permeability jumped up. Then the water phase became less mobile and relative permeability declined somewhat. Fractional flow was largely unaffected by the switch in miscibility as the increase in oil and water relative permeabilities seemed to cancel each other out.

Qualitatively similar behavior was observed in the base case (100 cell) model in cells 91 to 99 (See Fig. 10a and Fig. 10c). The cells are closer together so the changes in behavior occur more frequently and we magnify the PVI on the x-axis of the plots. The initial short rise in $\log(N_c)$ was observed in each cell followed by a sharp change as fluids became miscible. Then after that there was a change in relative permeabilities and fractional flow as viscosity changed. In this case, we see pulses in saturation and relative permeabilities as well as fractional flow. On top of that there seems to be a dual frequency of pulses. In cell 99, for example, there were some high frequency pulses just before the cell became miscible by the arrival of the surfactant. These high frequency pulses were also seen and correlated with behavior in the preceding cells. The high frequency pulses appeared to correlate with the change in $\log(N_c)$ in Fig 10c.

As mentioned above, Al Idadi et al. [28-30] have shown similar such pulses for low salinity waterflooding. In that case relative permeability is changed rapidly due to the reduction of salinity as injected water arrives. This process emulates a change in wettability. The change of relative permeability increases oil flow and reduces water flow. The resulting pulse in a cell can then propagate downstream and appear in saturation and fractional flow. The pulses were shown to grow in magnitude as the low salinity front arrived. In the numerical case, dispersion slowed down the increase of water saturation that is normally associated with the low salinity front in the analytical solution which depends on sharp fronts. In the latter case, saturation and salinity change together preventing the pulses. We hypothesize that the same process occurs here for surfactant flooding as oil becomes more mobile when miscibility changes. Water mobility was initially increased by the change of relative permeability but then decreased when the viscosity was reduced with increasing surfactant concentration. We observe the effects in the 100 cell model and in the water cut of the 10 cell model by the presence of the double bump before the surfactant water front arrived. Al Ibadi et al. [28-30] showed that the pulses grew in number as the formation and low salinity water fronts separated out. We observe the same here in longer models.

In earlier time, longer wavelength pulses were also observed in the fractional flow curve (but not in the water relative permeability curve). These appear as troughs which become deeper in time and have a periodicity of about 0.08 PVI (roughly the time for 10 cells to change from immiscible to miscible upstream). The troughs also correlate across cells. This effect was not reported for low salinity waterflooding. The grid refinement reduced the effect of numerical dispersion but there remain some numerical effects. We can conclude that the pulses were a result of the presence of multiple phases at a given point, where the upstream weighting of the relative permeability values produced unphysical pulses causing a ripple effect that was transmitted through the cells to the production well. Grid

refinement actually introduced more pulses but they were compressed and began to converge to the analytical solution. Al Ibadi et al. [28-30] showed that the number of ripples increased when cells were considered further from the injector because the formation and injected water fronts separate out. Refinement also saw pulses diminish in magnitude.

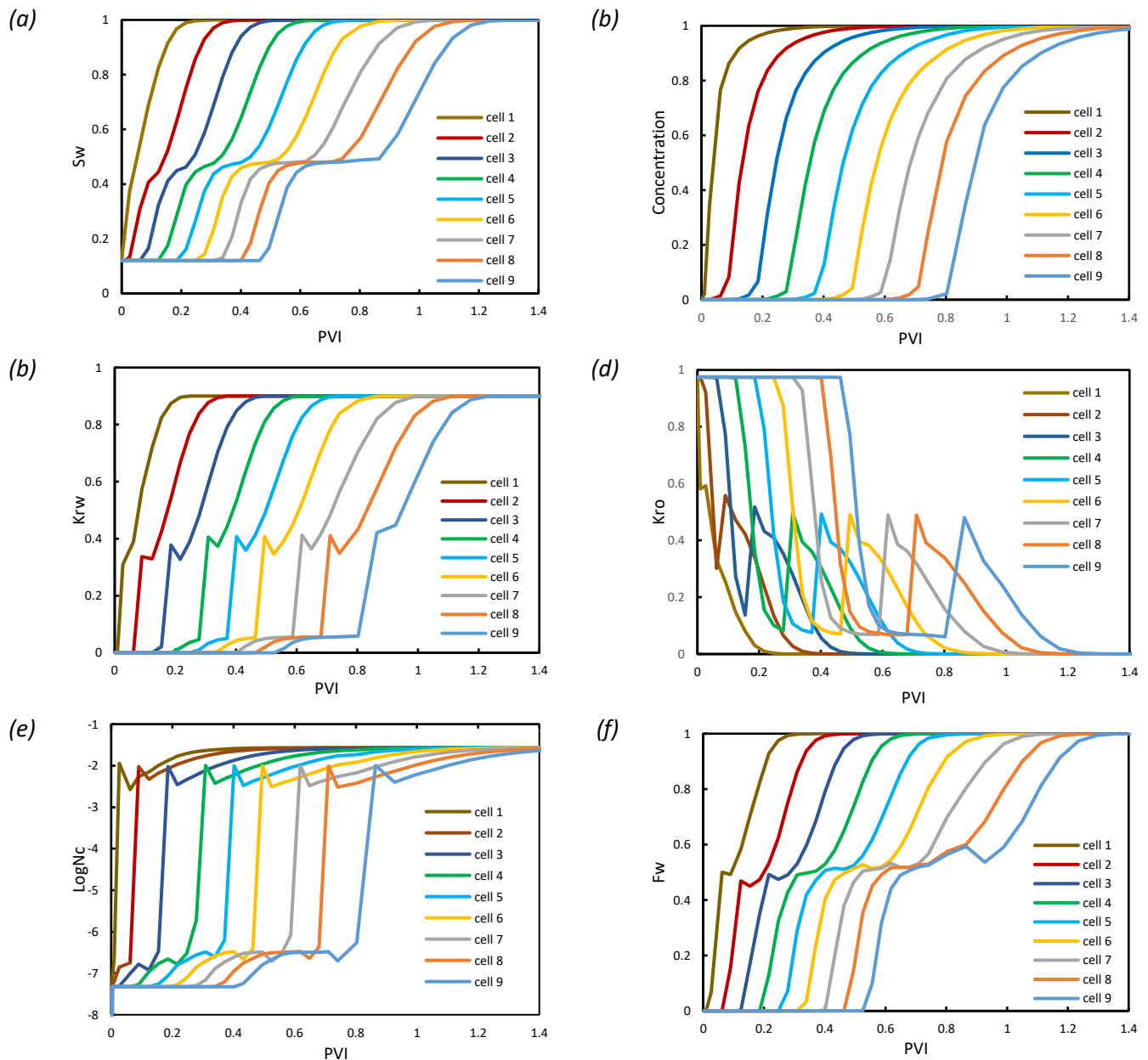


Fig. 9 Simulation output of the surfactant flood for the coarse model ($10 \times 1 \times 1$) as the fluid passes from the injector well (cell 1) to near the production well (cell 9) versus pore volume injected. For each cell we show (a) water saturation, (b) surfactant concentration (c) water relative permeability, (d) oil relative permeability, (e) The logarithm of the capillary number and for flow from cell i to $i+1$, (f) fractional flow. This analysis follows that presented in [28] and [30] for low salinity waterflooding with a similar hypothesis.

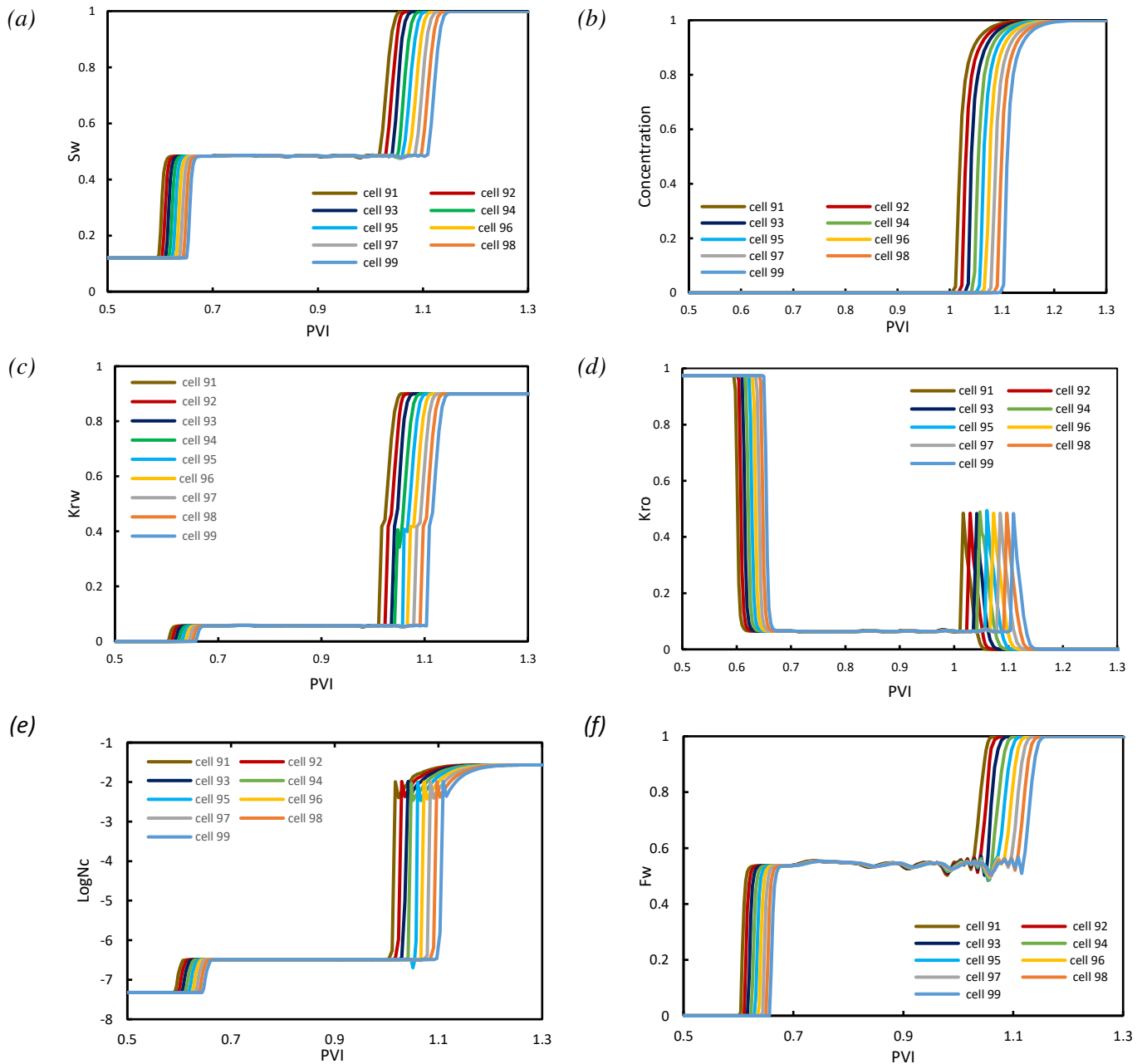


Fig. 10 Simulation output of the surfactant flood for the base case model ($100 \times 1 \times 1$) as the fluid passes from cell 91 to 99 indicating for each cell (a) water saturation, (b) surfactant concentration (c) water relative permeability, (d) oil relative permeability, (e) the logarithm of the capillary number and for flow from cell i to $i+1$, (f) fractional flow.

7 Time-step reduction and effect on the appearance of numerical effects

We examined the impact of time step reduction on the surfactant flood base case model concerning the appearance of numerical effect and computational efficiency. The base case grid block setup ($100 \times 1 \times 1$) was simulated with various time steps, corresponding Peclet number, and computational time (see Table 3).

We show in Fig. 11 that the time step contributes heavily to the numerical dispersion. The reference case ($N_{pe} = 40$) produced the noisiest, and with significant pulses spanning across the plateau in comparison with the other case studies. Reducing the time step to 1 day ($N_{pe} = 52$), 0.45 days ($N_{pe} = 64$) and 0.01 days ($N_{pe} = 80$) resulted in water cut solution profiles became more closely comparable to the high-resolution model ($N_{pe} = 2000$) and analytical solution (See Fig. 12).

Table 3 Computational times and Numerical Peclet number of the base case model ($\Delta x = 5m$) for time sensitivity.

Case ID	Δt (days)	N_{pe}	CPU Time (seconds)
Base Case / TIME01	1.82	40	76.1
TIME02	1	52	47.8
TIME03	0.45	64	66.1
TIME04	0.2	72	115.8
TIME05	0.01	80	2286.5

The computational efficiency of the solution profiles also was considered. The reference time step was seen to lack computational efficiency when compared with a time step of 1 day ($N_{pe} = 52$) and 0.45 days ($N_{pe} = 64$) (See Table 3). We did observe convergence issues with the Base Case. The increase of numerical dispersion seems to have exacerbated the issues, hence additional iterations were required as the problem became harder to solve.

Closer inspection of Fig. 12 reveals that the apparent long wavelength pulses were clearly an artifact of the dispersion as they were not present in any of the models with $N_{pe} > 40$. High frequency pulses were observed as the injected water front arrived but the plateau of the formation water front was mostly flat and equivalent to the analytical solution. An exception to this was the case of the time step of 0.2 days ($N_{pe} = 72$) which produced a solution profile with pulses but there was also a jump in water cut above the value of the analytical solution. Further investigation was required to underpin why the initial bump appeared in the solution profiles that were contrary to the analytical solution. We can conclude that to enhance the precision for the numerical modelling of the transport of surfactant flood weighed against the appearance of nonphysical solution and computational efficiency, the courant condition considered should be as follows:

$$\Delta t_{Max} \leq \frac{\Delta x}{2v} \quad (15)$$

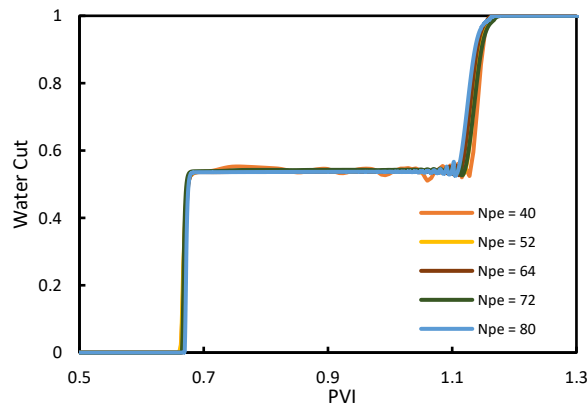


Fig. 11 A comparison of the water cut profile from the simulation results. The reference case $N_{pe} = 40$ (dark red line), $N_{pe} = 52$ (orange line), $N_{pe} = 64$ (brown line), $N_{pe} = 72$ (green line) and $N_{pe} = 80$ (blue line) accordingly.

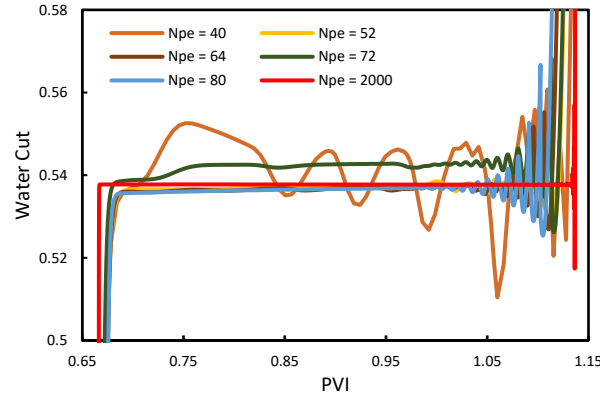


Fig. 12 A zoomed-in observation of the comparison of the appearance of numerical effects in the various value time step compared to the high-resolution model $N_{pe} = 2000$ (red line) considered as the most accurate representation of the analytical solution.

8 The effects of adsorption: impact of zero adsorption on oil recovery

We also examined how the variation of adsorption in the surfactant flood model affected recovery factor as a function of the different grid cell sizes. We ran the base case model that was used above with zero adsorption (Fig. 13). The analytical result was almost perfectly matched by the most refined model ($N_{pe} = 2000$) and oscillations appeared as the model was coarsened. We observed the appearance of an obvious dip in the water cut solution profile just ahead of the surfactant induced waterfront for $N_{pe} = 40$, the pulse had a different magnitude compared to the base case, which modelled adsorption. As described above, the dispersion of the surfactant initially changed the mobility of the water which changed relative permeability and caused the dip. Then the IFT decreased when the threshold of the capillary number was reached. The dip was largest for the coarsest grid which also saw a much earlier breakthrough of the formation water while other cases correctly predicted this. Overall the main effect of enlarging the cell size was to change the water cut and to predict earlier breakthrough of surfactant. The dispersed surfactant front moved faster than the formation water in the absence of adsorption (Fig. 13). This disturbed the formation water front which no longer moved at the same steps in saturation and fractional flow. Fig. 14 shows that, with the exception of the coarsest model, the cumulative volume of oil produced matches the analytical solution very well. The deviations are small compared to the cumulative volumes. We conclude that in the absence of adsorption, a more refined model is required to obtain sufficient precision.

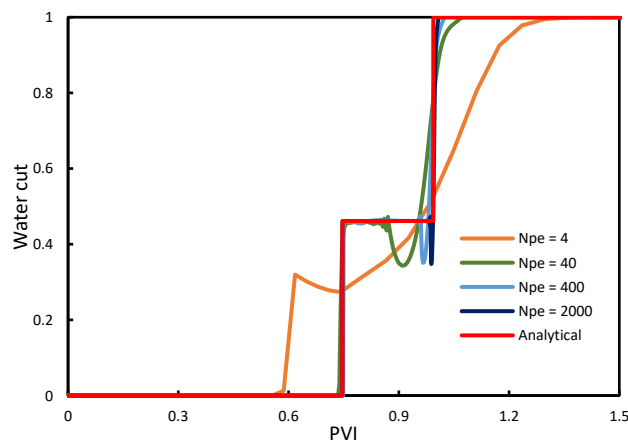


Fig. 13 a. A comparison of the impact of zero adsorption on the water cut profile verse pore volume injected for $N_{pe} = 4$ (orange line), $N_{pe} = 40$ (green line), $N_{pe} = 400$ (blue line), $N_{pe} = 2000$ (purple line) and analytical solution (red line).

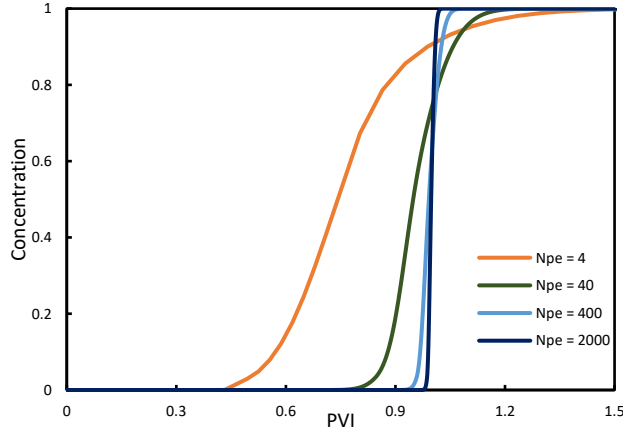


Fig. 13 b. A comparison of the dimensionless concentration profile versus pore volume injected for $N_{pe} = 4$ (orange line), $N_{pe} = 40$ (green line), $N_{pe} = 400$ (blue line), $N_{pe} = 5000$ (purple line).

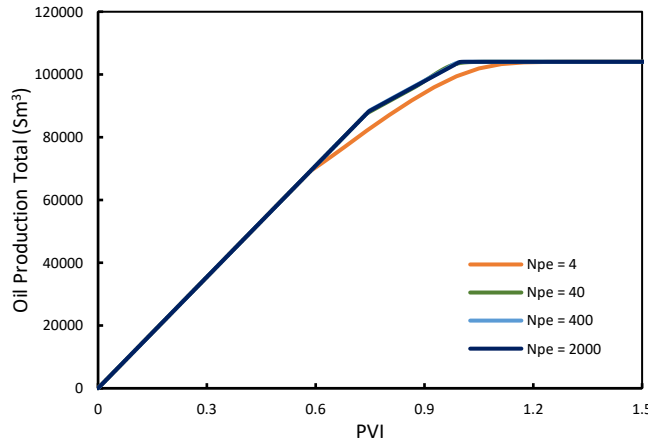


Fig. 14 A comparison of the oil recovery versus pore volume injected for $N_{pe} = 4$ (orange line), $N_{pe} = 40$ (green line), $N_{pe} = 400$ (blue line), and $N_{pe} = 2000$ (purple line).

9 Varying adsorptions

Lastly, we examined the role of the adsorption on the sharpening of the front and appearance of pulses in the numerical solutions. We used the base case model and made some modifications to the adsorption values for this study (See Table 4).

Table 4 Adsorption Simulation Input Parameters

Base Case Model	Δt_{Max} (days)	Case 1 (kg/kg)	Case 2 (kg/kg)	Case 3 (kg/kg)	Case 4 (kg/kg)	Case 5 (kg/kg)
100 x 1 x 1	1	0	0.1E-3	0.3E-3	0.5E-3	0.8E-3

The increase of the adsorption rates resulted in the acceleration of the formation waterfront and a retardation of the injected waterfront. Adsorption removed surfactant from the injected water so that it behaved like formation water. We can observe the impact of adsorption on the interpreted D_i achieved through the use of the Welge tangent on the fractional flow curve (See Fig. 3). We also saw a change in the numerical effects.

It was observed in the comparison between the water cut profile with zero adsorption through the appearance of an obvious dip (Fig. 15) that can be directly related to the pulse observed in the water relative permeability curves (Fig. 16), which was caused by the change of viscosity as the surfactant concentration rose to 1 kg Sm^{-3} . The relative permeability of water appeared to drop as the surfactant arrived and then increased as the oil was displaced. The dip in water cut gradually diminished when

adsorption was increased to 0.0003kg/kg; this was then followed by the recurrence of the pulses as the adsorption was further increased to 0.0005kg/kg. The interpretation of the second pulse on the solution profile may be caused by the appearance of the numerical effect observed during the mobilization of the formation water (Fig. 17), which was initially less mobile. As the adsorption rate was increased further, the surfactant concentration decreased. The decrease in the concentration lagged in the water solution displacement due to the pore volume that can be accessed by the surfactant; this caused the surfactant to move slowly and thus the initially immobile oil was released and recovered more quickly. We observed from the surfactant flood fractional flow curves from the simulator data which were computed as the producer cell first saw formation water invade then a change from the immiscible curves towards the surfactant induced miscible curves. The input fractional flow curves are shown as reference (Fig. 18). The waterflood initially appeared to correspond to the predicted fractional flow theory, while there also appeared to be complexity all along the curve prior to the transition to the miscible surfactant flood curve. This might be the reason for the appearance of the dip observed in the zero adsorption and 0.0001kg/kg value; which showed a jump and deviation from the waterflood curve in value of saturation and fractional flow due to the arrival of the surfactant concentration. From the theoretical analysis, the Welge tangent was used to understand the water saturation shock fronts of both the water formation and surfactant induced fronts. The two cases (zero adsorption and 0.0001kg/kg) appeared to have two possible tangent points, one along the waterflood curve and the deviated point that corresponds to the tangent point of the adsorption value of 0.0003kg/kg with less match of the water saturation. The dispersion had a clear impact on changing the shape of the curves making them less precise.

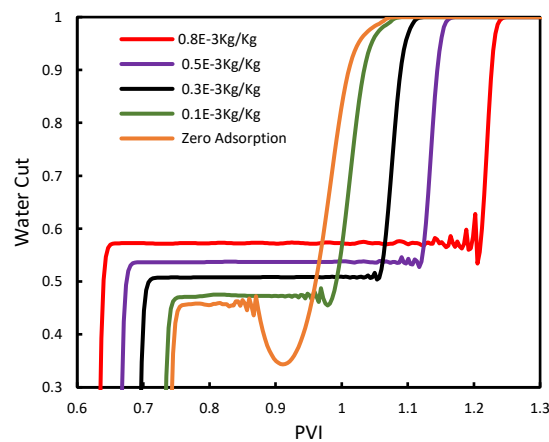


Fig. 15 The effect of adsorption sensitivity on the water cut profile from when adsorption was neglected (orange line) to 0.0008kg/kg (red line).

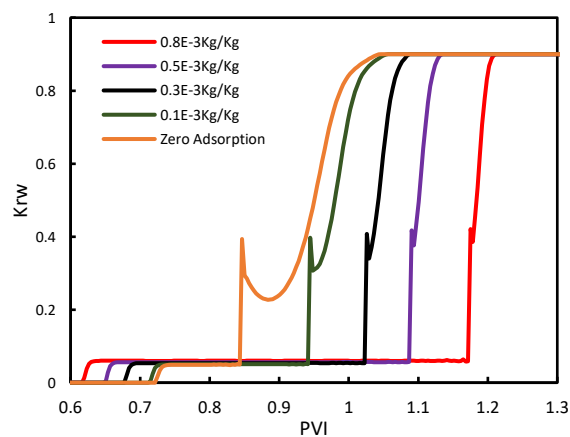


Fig. 16 The water relative permeability for the adsorption sensitivity versus pore volume injected.

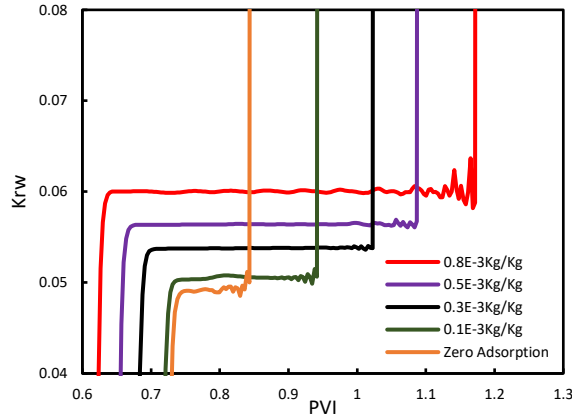


Fig. 17 A magnified observation of the pulses across the transition between connate water into the interstitial water relative permeability curve.

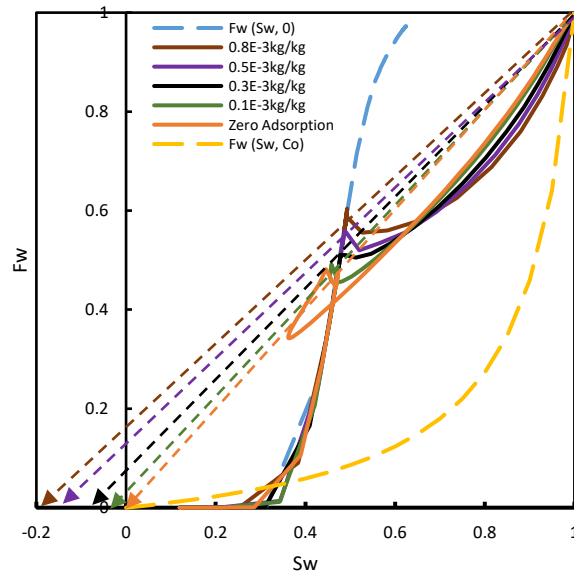


Fig. 18 The fractional flow curves obtained from simulator output of the various adsorption rates (solid lines) with derived analytical curves from input relative permeability curves (longer dashed lines). The Welge tangents for each case are shown (red short dashed lines) for each case by drawing the tangent to the miscible fractional flow curve through the maximum saturation on the formation water front.

10 Discussion

We have examined the stability, precision, computational efficiency, and effects of adsorption on the simulated surfactant flooding behaviour in a homogenous model at inter-well scale. We showed that grid refinement improves the precision of the surfactant concentration front, which was strongly affected in the coarse grid model and produced false predictions. The analytical solution was shown to be effective for characterizing the various surfactant models through relationships between the surfactant concentration, oil-water IFT, and effective solution viscosity to make a distinction between the degree of deviation and accuracy of the solution. Also, for finer grids, there was less numerical dispersion observed. The required computational times grew with the demand for precision and stability in the solution profile. As a means of optimizing the choice of grid cell, we used the courant condition to determine the maximum time step for the surfactant flood model. Imprecision problems occurred in the surfactant concentration front as dispersion dominated and where neither the advection nor dispersion dominated over another, particularly when the Peclet number was less than 40 for the

decoupled implicit scheme. Following the selection of an appropriate grid block structure for analysis, a decrease in the appearance of pulses was achieved through further reduction of the time step.

Key mechanisms influencing the surfactant flood model may be used to further understand the origin and the spread of the pulses. The switch in relative permeability seems to have been important as has been reported for low salinity waterflooding by Al-Ibadi et al. [28-30]. The numerical solution of the base case model with the modified Courant condition was tested according to various adsorption values derived using the Langmuir-type isotherm variable. Two different types of numerical effects were observed in this study. Pulses occurred at the secondary fronts, resulted in a stable and seemingly removed numerical effect after the adsorption rate increased above the value of 0.0002kg/kg. The first effect occurred when dispersion led to earlier change of viscosity and miscibility, triggered by the lack of adsorption in the surfactant flood model. This speed up the concentration front displacement. whereas, the numerical effects that gave rise to a stable solution, was formed by the mobilization of the formation water. An increase in adsorption boosted the magnitude of the pulses on the solution profile. Therefore, the presence of adsorption makes it easier to reduce the numerical effect as well and the precision of the surfactant flood solution tended to be better.

11 Conclusions

We conclude the following from this study:

- Numerical precision problems were identified for models with a typical cell size as used in well-scale models.
- Pulses were observed in the oil bank with multiple frequencies or duration.
- A dip in water saturation and fractional flow was observed for low levels of adsorption so that more refined models were needed.
- The Courant condition should be observed as a minimum to avoid these effects.

Also, we suggest further work is required to examine the relevance of these findings in the 2D and 3D layered and heterogeneous reservoir scale representation of the surfactant flood model.

Acknowledgments

The financial support from Nigerian Petroleum Technology Development Fund is greatly appreciated. We would like to thank Schlumberger for the application of Eclipse 100 simulator. We also thank Hasan Al-Ibadi for his contributions to discussions on pulses as seen previously in low salinity waterflooding.

References

1. Sun, Q., et al., *Utilization of Surfactant-Stabilized Foam for Enhanced Oil Recovery by Adding Nanoparticles*. Energy & Fuels, 2014. **28**(4): p. 2384-2394.
2. Abhishek, R., G.S. Kumar, and R.K. Sapru, *Wettability Alteration in Carbonate Reservoirs Using Nanofluids*. Petroleum Science and Technology, 2015. **33**(7): p. 794-801.
3. Druetta, P., et al., *Numerical modeling of a compositional flow for chemical EOR and its stability analysis*. Applied Mathematical Modelling, 2017. **47**: p. 141-159.
4. Schlumberger, *ECLIPSE 100*, in *Technical Description*, R. Manual, Editor. 2019, Schlumberger Reservoir Technologies
5. Hirasaki, G., C.A. Miller, and M. Puerto, *Recent Advances in Surfactant EOR*. SPE Journal, 2011. **16**(04): p. 889-907.
6. Pratt, J.D. and T.F. West, *Editors' Preface*, in *Surface Active Chemicals*, H.E. Garrett, Editor. 1972, Pergamon. p. ix-x.
7. Farrell, H.H., M.D. Gregory, and M.T. Borah, *Progress Report: Big Muddy Field Low-Tension Flood Demonstration Project With Emphasis on Injectivity and Mobility*, in *SPE Enhanced Oil Recovery Symposium*. 1984, Society of Petroleum Engineers: Tulsa, Oklahoma. p. 7.
8. Reppert, T.R., et al., *Second Ripley Surfactant Flood Pilot Test*, in *SPE/DOE Enhanced Oil Recovery Symposium*. 1990, Society of Petroleum Engineers: Tulsa, Oklahoma. p. 12.
9. Maerker, J.M. and W.W. Gale, *Surfactant flood process design for Loudon*. SPE (Society of Petroleum Engineers) Reservoir Engineering; (United States), 1992: p. Medium: X; Size: Pages: 36-44.
10. Green, D.W. and G.P. Willhite, *Enhanced oil recovery*. 1998, Richardson, TX: Henry L. Doherty Memorial Fund of AIME, Society of Petroleum Engineers.
11. Iglauer, S., et al., *New surfactant classes for enhanced oil recovery and their tertiary oil recovery potential*. Journal of Petroleum Science and Engineering, 2010. **71**(1): p. 23-29.
12. Sheng, J.J., *Status of surfactant EOR technology*. Petroleum, 2015. **1**(2): p. 97-105.
13. Larson, R.G., H.T. Davis, and L.E. Scriven, *Elementary Mechanisms of Oil Recovery by Chemical Methods*. Journal of Petroleum Technology, 1982. **34**(02): p. 243-258.
14. Daiyin, Y. and Z. Yazhou, *Numerical simulation of surfactant flooding and its application in low permeability reservoir*. International Journal of Control and Automation, 2013. **6**(4): p. 451-472.
15. Thomas, S. and S.M.F. Ali, *Micellar Flooding And ASP - Chemical Methods For Enhanced Oil Recovery*, in *Annual Technical Meeting*. 1999, Petroleum Society of Canada: Calgary, Alberta. p. 8.
16. Xu, F., et al., *Case Study: Numerical Simulation Of Surfactant Flooding In Low Permeability Oil Filed*, in *SPE Enhanced Oil Recovery Conference*. 2011, Society of Petroleum Engineers: Kuala Lumpur, Malaysia. p. 11.
17. Healy, R.N., R.L. Reed, and D.G. Stenmark, *Multiphase Microemulsion Systems*. Society of Petroleum Engineers Journal, 1976. **16**(03): p. 147-160.
18. Healy, R.N. and R.L. Reed, *Physicochemical Aspects of Microemulsion Flooding*, in *Fall Meeting of the Society of Petroleum Engineers of AIME*. 1973, Society of Petroleum Engineers: Las Vegas, Nevada. p. 20.
19. Pope, G.A. and R.C. Nelson, *A Chemical Flooding Compositional Simulator*. Society of Petroleum Engineers Journal, 1978. **18**(05): p. 339-354.
20. Nelson, R.C. and G.A. Pope, *Phase relationships in chemical flooding*. Journal Name: Soc. Pet. Eng. AIME, Pap.; (United States); Journal Volume: SPE-6773; Conference: 52. annual meeting of the Society of Petroleum Engineers, Denver, CO, USA, 9 Oct 1977. 1977: ; Shell Development Co. Medium: X; Size: Pages: 12.
21. Pope, G.A., *The application of fractional flow theory to enhanced oil recovery*. SOC. PET. ENGRS. J., 2017. **20**(3 , Jun. 1980): p. 191-205.
22. Buckley, S.E. and M.C. Leverett, *Mechanism of Fluid Displacement in Sands*. Transactions of the AIME, 1942. **146**(01): p. 107-116.

23. Fanchi, J.R., *Multidimensional Numerical Dispersion*. Society of Petroleum Engineers Journal, 1983. **23**(01): p. 143-151.
24. Lake, L.W., *Enhanced oil recovery*. 1989: Old Tappan, NJ; Prentice Hall Inc. Medium: X; Size: Pages: (550 p).
25. Al-Ibadi, H., K.D. Stephen, and E. Mackay, *Insights into the fractional flow of low salinity water flooding in the light of solute dispersion and effective salinity interactions*. Journal of Petroleum Science and Engineering, 2019. **174**: p. 1236-1248.
26. Lantz, R.B., *Rigorous Calculation of Miscible Displacement Using Immiscible Reservoir Simulators*. Society of Petroleum Engineers Journal, 1970. **10**(02): p. 192-202.
27. Sorbie, K. and E. Mackay, *Mixing of injected, connate and aquifer brines in waterflooding and its relevance to oilfield scaling*. Journal of Petroleum Science and Engineering, 2000. **27**: p. 85-106.
28. Al-Ibadi, H. H., Stephen, K. D., and Mackay, E. J. 2018 *Improved Numerical Stability and Upscaling of Low Salinity Water Flooding*. Presented at the SPE Asia Pacific Oil and Gas Conference and Exhibition, Brisbane, Australia, 23–25 October. 2018. SPE paper 192074-MS
29. Al-Ibadi, H. H., Stephen, K. D., and Mackay, E. J. 2021 *Pulse Generation and Propagation in the Numerical Solution of Low Salinity Water Flooding*. Journal of Petroleum Science and Engineering, In Press.
30. Al-Ibadi, H. H., Stephen, K. D., and Mackay, E. J. 2021 *An Analysis of Numerically Induced Pulses in Simulations of Low Salinity Water Flooding and their Reduction by Flow Upscaling*. Society of Petroleum Engineers Journal, In Press.
31. Adibhatla, B. and K.K.J. Mohanty, *Parametric analysis of surfactant-aided imbibition in fractured carbonates*. Journal of colloid and interface science, 2008. 317: p. 513-22.
32. Akin, S. and A. Kovscek, *Computed tomography in petroleum engineering research*. Geological Society, London, Special Publications, 2003. 215: p. 23-38.